

Topological superconductivity in a phase-controlled Josephson junction

Hechen Ren^{1,2}, Falko Pientka^{1,3}, Sean Hart^{1,4}, Andrew T. Pierce¹, Michael Kosowsky¹, Lukas Lunczer⁵, Raimund Schlereth⁵, Benedikt Scharf⁶, Ewelina M. Hankiewicz⁶, Laurens W. Molenkamp⁵, Bertrand I. Halperin¹ & Amir Yacoby^{1*}

Topological superconductors can support localized Majorana states at their boundaries^{1–5}. These quasi-particle excitations obey non-Abelian statistics that can be used to encode and manipulate quantum information in a topologically protected manner^{6,7}. Although signatures of Majorana bound states have been observed in one-dimensional systems, there is an ongoing effort to find alternative platforms that do not require fine-tuning of parameters and can be easily scaled to large numbers of states^{8–21}. Here we present an experimental approach towards a two-dimensional architecture of Majorana bound states. Using a Josephson junction made of a HgTe quantum well coupled to thin-film aluminium, we are able to tune the transition between a trivial and a topological superconducting state by controlling the phase difference across the junction and applying an in-plane magnetic field²². We determine the topological state of the resulting superconductor by measuring the tunnelling conductance at the edge of the junction. At low magnetic fields, we observe a minimum in the tunnelling spectra near zero bias, consistent with a trivial superconductor. However, as the magnetic field increases, the tunnelling conductance develops a zero-bias peak, which persists over a range of phase differences that expands systematically with increasing magnetic field. Our observations are consistent with theoretical predictions for this system and with full quantum mechanical numerical simulations performed on model systems with similar dimensions and parameters. Our work establishes this system as a promising platform for realizing topological superconductivity and for creating and manipulating Majorana modes and probing topological superconducting phases in two-dimensional systems.

Majorana bound states (MBS) are quasiparticle excitations that are their own antiparticles and hence can serve as the basis of topological quantum computing, where quantum information can be stored and manipulated robustly^{6,23}. Spectroscopic studies have been conducted in various one-dimensional systems, such as proximitized nanowires and atomic chains, where zero-bias peaks exist in the tunnelling spectra in parts of the parameter space associated with MBS^{10–12,14–21}. Despite the growing evidence, scalable networks of Majorana qubits are challenging to obtain in such one-dimensional platforms, owing to both the intrinsic instabilities associated with one-dimensional systems and the technological obstacles in their physical implementation^{13,24}. Therefore, to understand and use the full power of MBS physics, two-dimensional platforms that can realize topological superconductivity are in demand for patterning large-scale networks of Majorana devices, as well as integrating them with other quantum information devices and systems, in a reproducible and controlled fashion²⁵.

We design and implement a controllable two-dimensional platform for realizing topological superconductivity. This platform is based on a recent theoretical proposal for a planar Josephson junction created from a two-dimensional electron gas (2DEG) subject to a strong Rashba spin–orbit interaction, sandwiched between two aluminium

superconducting leads²² (Fig. 1a). In this system, the phase transition between trivial and topological superconductivity can be tuned using two independent knobs: the phase difference across the junction, ϕ , and the Zeeman energy E_Z , which is governed by an external magnetic field applied in the plane of the junction. In a long Josephson junction that is translationally invariant along x , the direction parallel to the superconducting electrodes, supercurrent is carried by bands of Andreev bound states in the normal (non-superconducting) region, formed by successive Andreev reflections at the normal–superconductor interfaces^{26,27}. The energy of each Andreev state thus depends both on ϕ and on the phase accumulated by the quasiparticles traversing the junction at various angles from the x direction. Therefore, the Andreev states can have a full range of wavevectors, with the x -components of their wavenumbers k_x varying in magnitude from 0 to nearly the Fermi wavenumber k_F . Their energies hence disperse to form a continuous sub-gap spectrum. Notably, when normal reflection at the normal–superconductor interface is weak, these Andreev bands are relatively flat and disperse only weakly with changing k_x (Fig. 1e). This leads to a strongly enhanced density of states near zero energy in the vicinity of the topological phase transition. When normal reflection is taken into account, the bands acquire a non-zero width (Fig. 1f).

A topological phase transition in a clean junction is accompanied by a zero-energy crossing at $k_x = 0$ (Fig. 1b). When the Zeeman energy is zero, the $k_x = 0$ Andreev states are two-fold degenerate and cross at $\phi = \pi$ in the absence of normal reflections. A finite magnetic field parallel to the x axis separates the $k_x = 0$ states by a phase difference $\Delta\phi = 2\pi E_Z/E_T$, where $E_T = (\pi/2)(\hbar v_F/W)$ is the Thouless energy (\hbar is the reduced Planck constant, v_F is the Fermi velocity, and W is the width of the junction.). In the range of ϕ values between these two crossings, the occupancy of fermionic states becomes odd, and the system undergoes a phase transition into a topological superconducting phase. We can map out this phase boundary in the ϕ – E_Z space (Fig. 1c). As E_Z increases from 0 to the Thouless energy E_T , the junction becomes topological in a growing range of ϕ values, with predicted MBS on the end of a semi-infinite junction. As E_Z further increases beyond E_T , this ϕ range starts to decrease, forming overall diamond shapes (dashed lines in Fig. 1c). In a physical system, normal reflection can occur at the interfaces, which hybridize the left- and right-moving modes in the junction and shift the phase boundary from the ideal scenario. In this case, the topological phase occupies regions deformed from the diamond shape, but its dependence on the magnetic field and the phase difference is robust (solid colour in Fig. 1c) and largely insensitive to changes in geometry and in electron chemical potential. Consequently, for a wide range of magnetic fields, the application of a small phase bias can easily tune the system in and out of the topological superconducting phase and is hence a powerful experimental knob that can be controlled in a rapid manner.

Our planar Josephson junction consists of an 8-nm-wide HgTe quantum well contacted by thermally evaporated aluminium leads about 15 nm thick, with 5 nm of titanium as a sticking layer. The junction

¹Department of Physics, Harvard University, Cambridge, MA, USA. ²Institute for Quantum Information and Matter, California Institute of Technology, Pasadena, CA, USA. ³Max-Planck-Institut für Physik komplexer Systeme, Dresden, Germany. ⁴IBM T. J. Watson Research Center, Yorktown Heights, NY, USA. ⁵Physikalisches Institut (EP3) and Institute for Topological Insulators, Universität Würzburg, Würzburg, Germany. ⁶Institut für Theoretische Physik und Astrophysik und Würzburg-Dresden Cluster of Excellence ct.qmat, Universität Würzburg, Würzburg, Germany.

*e-mail: yacoby@q.harvard.edu

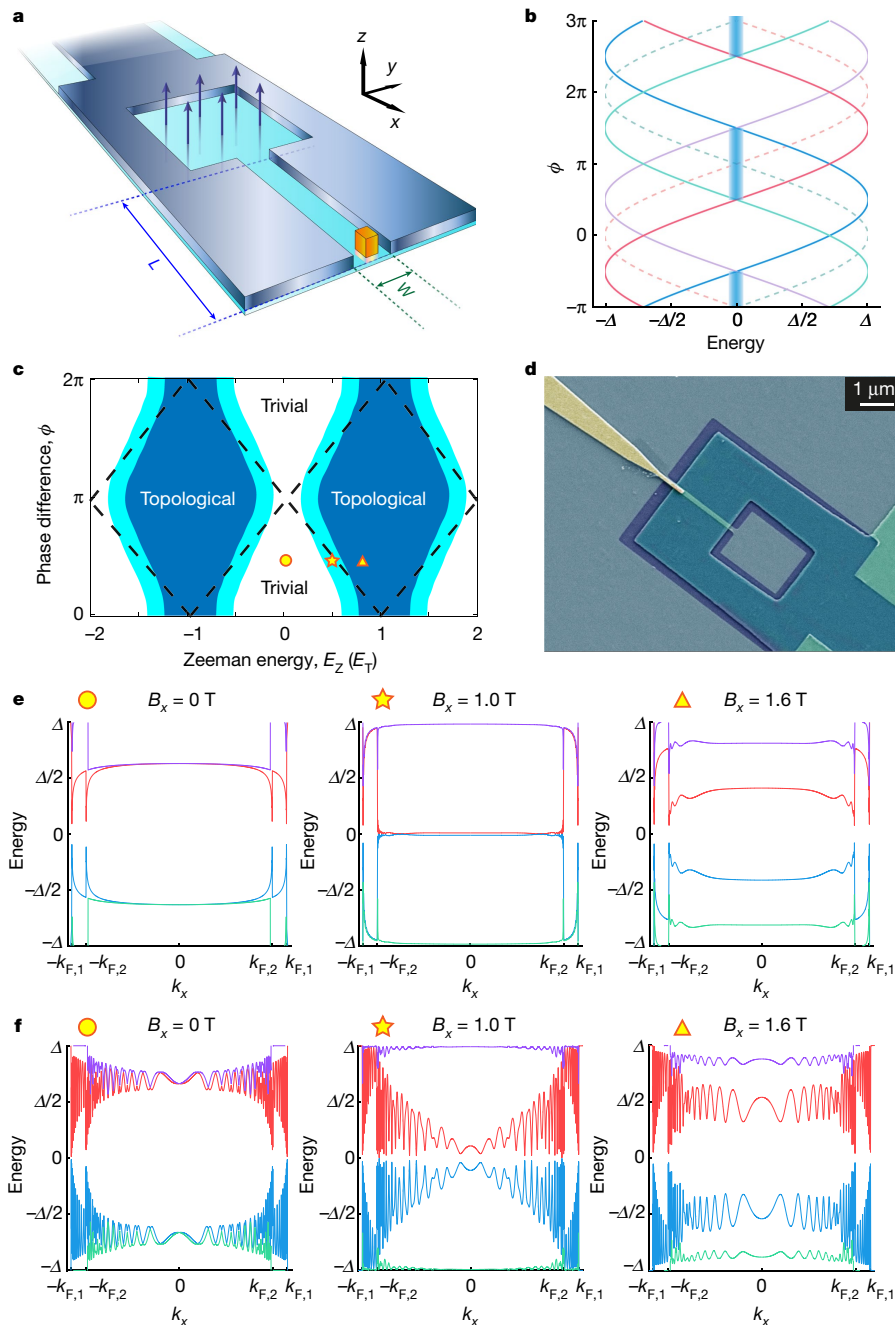


Fig. 1 | Topological transition in a phase-controlled Josephson junction. **a**, Device schematic for a planar Josephson junction of length L and width W created from a HgTe 2DEG (cyan) sandwiched between two aluminium superconducting leads, the ends of which connect to form a flux loop (steel blue). (We made devices both with and without the hole inside the flux loop and found little difference between the two designs. Data presented in the main text were taken from a device with a wider junction (600 nm) and without the hole in the mesa.) The tip of the tunnel probe (gold) overlaps with the 2DEG and is separated from it by a region of CdHgTe (pastel colours below the tip). The perpendicular component of the external magnetic field B_z is used to tune the phase difference across the junction. **b**, The bound-state spectrum (in units of the induced superconducting gap Δ) for $k_x = 0$ for a junction that is long in the x direction and symmetric in the y direction. The state is two-fold degenerate in the absence of any external magnetic field (dashed lines), and spin-split in the presence of an in-plane field (solid lines), accommodating a topological phase that

develops in the range of ϕ values between the zero-bias crossings (blue shaded regions). **c**, The boundary between the topological and trivial phases' superconductivity in the ϕ - E_z space. Normal reflection at the superconducting-normal interface can cause it to deviate (light blue ribbons) from the diamond shapes (dashed lines) that correspond to the case of perfect transparency. **d**, False-colour scanning electron micrograph of a device with a narrow junction. The mesa region containing the 2DEG is coloured in green, the superconducting contact is purple and the tunnel probe is yellow. **e**, Dispersion of the Andreev band as a function of k_x , at three values of Zeeman energy ($k_{F,1}$, $k_{F,2}$ are the Fermi momenta of the two spin components). The circle, star and triangle correspond to the regions in **c**. The Andreev bands become relatively flat during the topological phase transition (middle panel). **f**, Including some normal reflection in the calculations shown in **e** results in a finite width of the bands. Solid lines in red, blue, purple and green in **b**, **e**, **f** represent spin-up and spin-down electrons and holes, respectively.

region is 600 nm wide and about 1 μm long, with one end of each lead connected to form a flux loop. As previously established, our HgTe quantum well, grown by molecular beam epitaxy, provides a 2DEG with

high mobility and dominant Rashba spin-orbit coupling, and the thin aluminium leads can superconduct up to 1.8 T of in-plane magnetic fields^{28,29}.

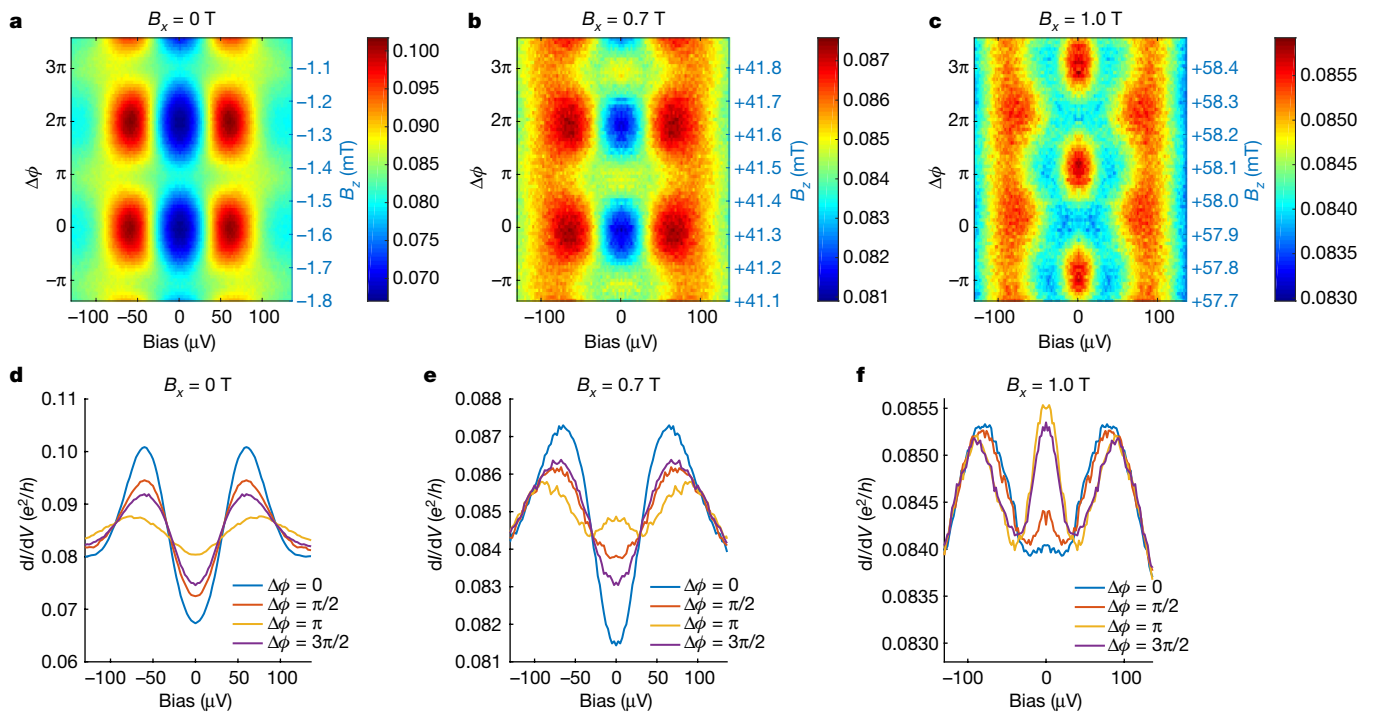


Fig. 2 | Phase modulations of the tunnelling conductance at low and high fields. **a–c**, Differential conductance colour plots (in units of e^2/h ; e , electron charge; h , Planck constant) as a function of the bias voltage (horizontal axis) and the phase difference (left vertical axis) offset from the $\Delta\phi = 0$ point, identified by the value of ϕ at which the coherence peaks reach a maximum. The right vertical axis shows the actual B_z field produced by the magnet. **d–f**, Line cuts of **a–c** showing the differential

conductance curves as a function of the bias voltage on the tunnel probe at four representative phase differences, averaged over repeating lines spaced at integer periods. **a, d**, Data taken at $B_x = 0$ T, where no zero-bias peak exists for any phase difference. **b, e**, Data taken at $B_x = 0.7$ T, where a zero-bias peak exists for a range of phase differences within each period. **c, f**, Data taken at $B_x = 1.0$ T, where a zero-bias peak persists through most of the period.

Using our vector magnet, we apply a magnetic field B_z perpendicular to the sample plane to generate the flux that controls the phase difference across the junction, and an in-plane magnetic field B_x in the x direction to tune the Zeeman energy (Fig. 1a, d). On the outer edge of the junction, we fabricate a weakly coupled electrode by evaporating 10 nm of titanium and 100 nm of gold, with approximately 10 nm of CdHgTe as a tunnel barrier, which is immediately above the HgTe layer in the MBE-grown heterostructure. The overlapping area is approximately $100 \text{ nm} \times 100 \text{ nm}$, which gives a tunnelling resistance of around 300 k Ω .

By applying an a.c. excitation in addition to a d.c. voltage bias on the tunnel probe and measuring the a.c. current through the superconducting lead, we can obtain a two-terminal differential conductance curve as we vary the d.c. bias. The observed spectrum of the proximitized 2DEG typically exhibits two broad coherence peaks separated by about 120 μV in bias voltage and a valley near zero bias (Fig. 2a). To see how the spectrum disperses with the phase difference ϕ , we scan B_z over a range of a few milliteslas near zero and record the differential conductance as a function of both the bias voltage and B_z . As shown by the colour maps in Fig. 2a–c, the tunnelling spectrum exhibits a strong periodic modulation with B_z , where the period matches the area of the flux loop, considering the magnetic flux repelled by the superconducting lead. The in-plane field also generates an asymmetry between positive and negative voltage biases, which we attribute to a particle–hole asymmetry. To highlight the contribution to the tunnelling conductance near zero energy, we symmetrize the data at positive and negative biases (the raw data and further discussion are presented in Supplementary Information section 3).

At low in-plane fields, the tunnelling spectra reveal a conductance minimum near zero bias, irrespective of the applied phase difference across the junction. This behaviour (Fig. 2a, b) resembles recent measurements in a graphene Josephson junction and is interpreted as the behaviour of the bulk Andreev bound states and their dependence on

the phase difference across the junction³⁰. We attribute the missing zero-bias conductance peak at low in-plane fields near a phase difference of π to the presence of weak normal reflections at the normal–superconducting interface. At high in-plane fields, a conductance peak develops near zero bias over a range of ϕ values, repeating periodically (Fig. 2c, f). The emergence of a robust and extended zero-bias peak in ϕ indicates the spectrum of the sub-gap states that concentrate near zero energy and persist over a wider range of ϕ values as the in-plane magnetic field increases (Fig. 3a–h).

To fully capture how the phase range containing the zero-bias peak grows with the magnetic field, we quantify the emergence of this conductance peak by extracting the curvature of the differential conductance curve around zero bias by using a parabolic fit on the raw data (Fig. 3i). We perform this analysis at all values of phase difference ϕ and in-plane field B_x to produce a colour map illustrating the development of the zero-bias peak in the ϕ – B_x phase space (Fig. 3i). At low fields, most ϕ values give a dip (positive curvature) in the zero-bias conductance, shown in red in Fig. 3i, indicative of a conventional superconducting phase. As B_x increases, the differential conductance becomes flatter near zero bias, and the parabolic fit yields a small absolute value, giving rise to a white region in the colour plot, which expands to occupy higher fractions of each period in ϕ . As the magnetic field continues to grow from 0.6 T to 1.2 T, the blue region of negative curvature emerges, marking the zero-bias peak, and expands to fill the entire period. Similar behaviour of the expanding zero-bias-peak region is observed for negative values of B_x , resulting in a phase diagram that is consistent with the predicted topological phase transition (Fig. 1c).

To simulate transport through the device, we describe the semiconductor by a tight-binding model with uniform Rashba spin–orbit coupling defined in a rectangular region. The region comprises a normal part sandwiched between two segments with proximity-induced superconductivity held at different phases (Supplementary Fig. 14; similar to Fig. 1a). We evaluate the conductance between a metallic tunnelling

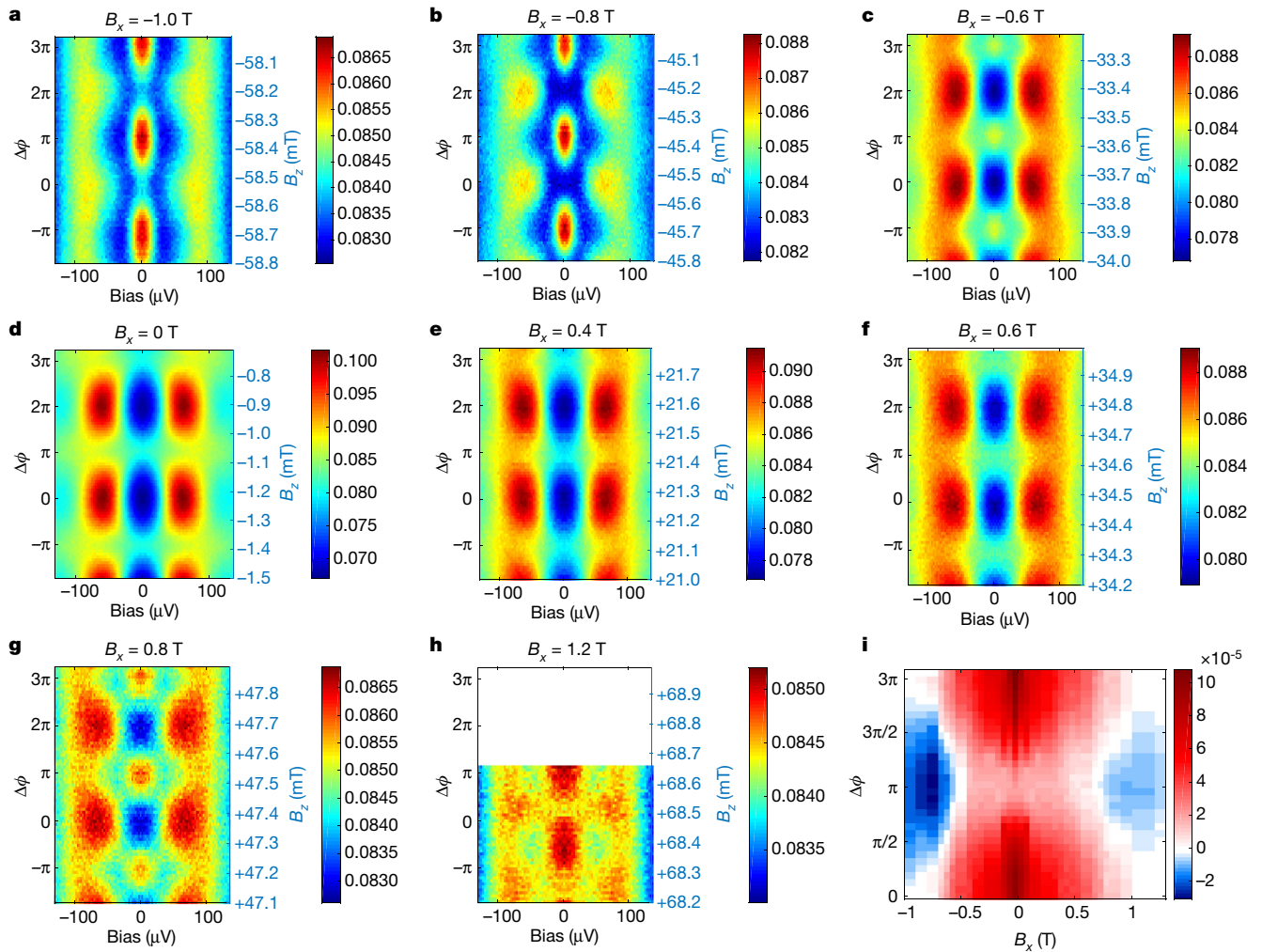


Fig. 3 | Development of a zero-bias peak and reconstructed phase diagram. **a–h**, Progression of tunnelling conductance colour plots (in units of e^2/h) as the magnetic field B_x varies from -1.0 T to 1.2 T, omitting the field values shown in Fig. 2 except for $B_x = 0$ T, which serves as a point of reference. All plots span over a range of 0.8 mT in B_z , except $B_z = 1.2$ T. **i**, Colour plot showing the extracted zero-bias curvature (in units of

$e^2 h^{-1} \mu\text{eV}^{-2}$) as a function of both the in-plane magnetic field B_x and the phase difference offset $\Delta\phi$. The blue region in the phase diagram shows where a well defined zero-bias peak is present in the tunnelling conductance. Its emergence and expansion with the application of both positive and negative in-plane magnetic fields agrees with the predicted phase transition (Fig. 1c).

probe attached to the edge of the normal region and two grounded superconducting leads that contact the superconducting regions on both sides, employing a scattering-matrix approach using the KWANT package³¹.

Motivated by the experimental observation that the superconducting coherence peaks do not shift in energy with the in-plane magnetic field, we assume a suppressed g factor in the proximitized parts and neglect the Zeeman field outside the normal region. Our model includes doping of the semiconductor due to the superconductor by assuming a higher density in the proximitized parts of the former. We account for the experimental resolution and non-uniform phase differences across the junction due to flux focusing by artificially broadening the theoretical data in energy and phase.

The calculated conductance, plotted as a function of bias voltage and phase in Fig. 4a–f, reproduces key features of the experimental data. At low Zeeman fields, the heights of the coherence peaks at $V \approx \pm 70 \mu\text{V}$ are modulated in phase and the conductance has a dip at zero bias for all values of the phase. At fields above $B_x = 0.5$ T, a peak at zero bias develops while the coherence peaks remain visible. In a minor deviation from the experiment, the coherence peaks shift to slightly higher energies $V \approx \pm 100 \mu\text{V}$ in the numerical simulations, which can be reconciled by accounting for a small gap suppression by the Zeeman effect in the superconductor.

The emergence of the zero-bias peak at finite fields is clearly visible in Fig. 4g, in which the curvature of the zero-bias conductance with bias voltage is plotted as a function of phase difference and the magnetic field. In the experimental field range, the numerical results in Fig. 4g are in excellent agreement with the experimental data in Fig. 3i. For all phase differences, the curvature monotonously decreases with the in-plane field and eventually transitions from a dip to a peak. At $B_x = 1$ T, a zero-bias peak exists for all values of the phase.

Comparing the theoretical curvature plot in Fig. 4g with the phase diagram in Fig. 1c reveals that the most pronounced zero-bias peaks occur close to the topological phase boundaries. At the same time, a zero-bias dip exists deep inside the topological phase. This is consistent with our numerical findings that the Majorana wavefunction is almost completely delocalized over the junction area for the experimental sample dimensions (see Supplementary Information section 7), precluding a dominant Majorana signature in the measurement. Instead, the peak originates from a band of quasi-one-dimensional sub-gap states living inside the junction (Fig. 1e). The density of states is enhanced at low energies as the band crosses zero energy in the vicinity of the topological phase transition, which manifests itself as a zero-bias conductance peak when the energy broadening is larger than the induced gap in the quasi-one-dimensional band. In the presence of normal reflection, the band acquires a finite width (Fig. 1f), and the zero-bias conductance

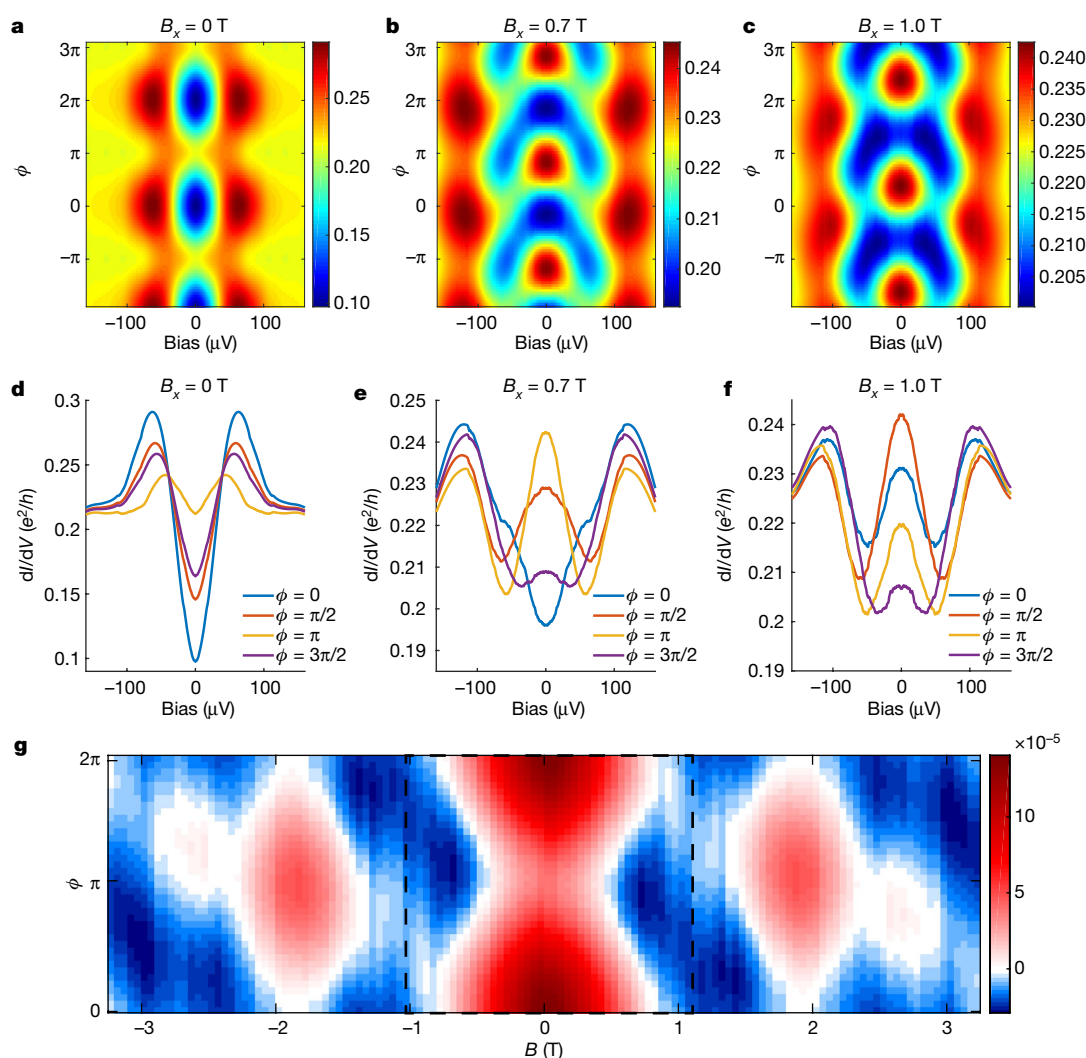


Fig. 4 | Numerical simulation of the tunnelling conductance using a tight-binding model. **a–c**, Calculated tunnelling conductance between a metallic tunnelling probe attached to the edge of the normal region and two grounded superconducting leads. **d–f**, Line cuts at four representative phase differences, taken from the conductance colour plots **a–c**, at three B_x fields corresponding to those shown in Fig. 2. The emergence of the zero-bias peak in finite fields agrees with the experimental data.

g, Predicted zero-bias curvature of the tunnelling conductance (in units of $e^2 h^{-1} \mu\text{eV}^{-2}$) as a function of both the in-plane magnetic field, B , and the phase difference, ϕ . Indicative of a zero-bias peak, the blue regions trace out the transition between the trivial and topological superconducting phases. Outlined in black dashed lines is the regime corresponding to the experimental data.

peak can exist in a broader parameter window around the phase transition (see Supplementary Information section 8 for a discussion about the density of states).

Future directions to improve this platform include enhancing the interface quality and adopting narrower and longer junctions, which will result in a harder gap in the junction (that is, stronger signals in the observed spectrum, such as a deeper dip or sharper contrast in the tunnelling conductance) and enable robust control of the topological transition without requiring higher magnetic fields (see Supplementary Information section 10). Notably, our approach does not rely on any fine-tuning of the chemical potential or the in-plane magnetic field and can be easily generalized to other two-dimensional materials, where the interplay of phase bias, spin–orbit coupling and Zeeman effect can create exciting opportunities to investigate topological superconductivity.

Data Availability

The data that support the findings of this study are available within the paper and its Supplementary Information. Additional data are available from the corresponding author upon request.

Online content

Any methods, additional references, Nature Research reporting summaries, source data, statements of data availability and associated accession codes are available at <https://doi.org/10.1038/s41586-019-1148-9>.

Received: 5 September 2018; Accepted: 14 February 2019;

Published online 24 April 2019.

1. Kitaev, A. Y. Unpaired Majorana fermions in quantum wires. *Phys. Uspekhi* **44**, 131–136 (2001).
2. Lutchyn, R. M., Sau, J. D. & Das Sarma, S. Majorana fermions and a topological phase transition in semiconductor–superconductor heterostructures. *Phys. Rev. Lett.* **105**, 077001 (2010).
3. Oreg, Y., Refael, G. & von Oppen, F. Helical liquids and Majorana bound states in quantum wires. *Phys. Rev. Lett.* **105**, 177002 (2010).
4. Alicea, J. New directions in the pursuit of Majorana fermions in solid state systems. *Rep. Prog. Phys.* **75**, 076501 (2012).
5. Beenakker, C. W. J. Search for Majorana fermions in superconductors. *Annu. Rev. Condens. Matter. Phys.* **4**, 113–136 (2013).
6. Kitaev, A. Y. Fault-tolerant quantum computation by anyons. *Ann. Phys.* **303**, 2–30 (2003).
7. Nayak, C., Simon, S. H., Stern, A., Freedman, M. & Das Sarma, S. Non-Abelian anyons and topological quantum computation. *Rev. Mod. Phys.* **80**, 1083–1159 (2008).

8. Stanescu, T. D., Lutchyn, R. M. & Das Sarma, S. Majorana fermions in semiconductor nanowires. *Phys. Rev. B* **84**, 144522 (2011).
9. Mourik, V. et al. Signatures of Majorana fermions in hybrid superconductor-semiconductor nanowire devices. *Science* **336**, 1003–1007 (2012).
10. Zhang, H. et al. Quantized Majorana conductance. *Nature* **556**, 74–79 (2018).
11. Nadj-Perge, S. et al. Observation of Majorana fermions in ferromagnetic atomic chains on a superconductor. *Science* **346**, 602–607 (2014).
12. Li, J., Neupert, T., Bernevig, B. A. & Yazdani, A. Manipulating Majorana zero modes on atomic rings with an external magnetic field. *Nat. Commun.* **7**, 10395 (2016).
13. Shabani, J. et al. Two-dimensional epitaxial superconductor–semiconductor heterostructures: a platform for topological superconducting networks. *Phys. Rev. B* **93**, 155402 (2016).
14. Rokhinson, L. P., Liu, X. & Furdyna, J. K. The fractional a.c. Josephson effect in a semiconductor–superconductor nanowire as a signature of Majorana particles. *Nat. Phys.* **8**, 795–799 (2012).
15. Churchill, H. O. H. et al. Superconductor-nanowire devices from tunneling to the multichannel regime: zero-bias oscillations and magnetoconductance crossover. *Phys. Rev. B* **87**, 241401 (2013).
16. Das, A. et al. Zero-bias peaks and splitting in an Al–InAs nanowire topological superconductor as a signature of Majorana fermions. *Nat. Phys.* **8**, 887–895 (2012).
17. Finck, A. D. K., Van Harlingen, D. J., Mohseni, P. K., Jung, K. & Li, X. Anomalous modulation of a zero-bias peak in a hybrid nanowire-superconductor device. *Phys. Rev. Lett.* **110**, 126406 (2013).
18. Albrecht, S. M. et al. Exponential protection of zero modes in Majorana islands. *Nature* **531**, 206–209 (2016).
19. Chen, J. et al. Experimental phase diagram of zero-bias conductance peaks in superconductor/semiconductor nanowire devices. *Sci. Adv.* **3**, e1701476 (2017).
20. Deng, M. T. et al. Majorana bound state in a coupled quantum-dot hybrid-nanowire system. *Science* **354**, 1557–1562 (2016).
21. Gül, Ö. et al. Ballistic Majorana nanowire devices. *Nat. Nanotechnol.* **13**, 192–197 (2018).
22. Pientka, F. et al. Topological superconductivity in a planar Josephson junction. *Phys. Rev. X* **7**, 021032 (2017).
23. Majorana, E. A symmetric theory of electrons and positrons. *Nuovo Cimento* **14**, 171–184 (1937).
24. Karzig, T. et al. Scalable designs for quasiparticle-poisoning-protected topological quantum computation with Majorana zero modes. *Phys. Rev. B* **95**, 235305 (2017).
25. Delfanazari, K. et al. On-chip Andreev devices: hard superconducting gap and quantum transport in ballistic Nb–In_{0.75}Ga_{0.25}As-quantum-well–Nb Josephson junctions. *Adv. Mater.* **29**, 1701836 (2017).
26. Andreev, A. F. The thermal conductivity of the intermediate state in superconductors. *Sov. Phys. JETP* **19**, 1228–1231 (1964).
27. Beenakker, C. W. J. & van Houten, H. Josephson current through a superconducting quantum point contact shorter than the coherence length. *Phys. Rev. Lett.* **66**, 3056–3059 (1991).
28. Hart, S. et al. Induced superconductivity in the quantum spin Hall edge. *Nat. Phys.* **10**, 638–643 (2014).
29. Hart, S. et al. Controlled finite momentum pairing and spatially varying order parameter in proximitized HgTe quantum wells. *Nat. Phys.* **13**, 87–93 (2017).
30. Brethau, L. et al. Tunnelling spectroscopy of Andreev states in graphene. *Nat. Phys.* **13**, 756–760 (2017).
31. Groth, C. W., Wimmer, M., Akhmerov, A. R. & Waintal, X. Kwant: a software package for quantum transport. *New J. Phys.* **16**, 063065 (2014).

Acknowledgements This work is supported by the NSF DMR-1708688, by the STC Center for Integrated Quantum Materials under NSF grant number DMR-1231319, and by the NSF GRFP under grant DGE1144152. This work is also partly supported by the US Army Research Office and was accomplished under grant W911NF-18-1-0316. The views and conclusions contained in this document are those of the authors and should not be interpreted as representing the official policies, either expressed or implied, of the Army Research Office or the US Government. The US Government is authorized to reproduce and distribute reprints for Government purposes notwithstanding any copyright notation herein. A.T.P. is supported by the US Department of Defense through the National Defense Science and Engineering Graduate Fellowship Program. The work at the University of Würzburg is supported by the German Research Foundation (Leibniz Program, Sonderforschungsbereich 1170 'ToCoTronics'; Würzburg-Dresden Cluster of Excellence on Complexity and Topology in Quantum Matter, ct.qmat, EXC 2147, project 39085490), the EU ERC-AG programme (Project 4-TOPS) and the Bavarian Ministry of Education, Science and the Arts (IDK Topologische Isolatoren and ITI research initiative).

Reviewer information *Nature* thanks Kaveh Delfanazari and the other anonymous reviewer(s) for their contribution to the peer review of this work.

Author contributions The experiment is a collaboration between the Harvard and Würzburg experimental groups. A.Y. conceived the experiment and supervised the project. L.L., R.S. and L.W.M. grew the material. H.R., S.H. and A.T.P. fabricated the devices. H.R., S.H., A.T.P. and M.K. performed the measurements. H.R., F.P., B.S., E.M.H., B.I.H. and A.Y. carried out the theoretical modelling and analysis and prepared the manuscript and Supplementary Information.

Competing interests The authors declare no competing interests.

Additional information

Supplementary information is available for this paper at <https://doi.org/10.1038/s41586-019-1148-9>.

Reprints and permissions information is available at <http://www.nature.com/reprints>.

Correspondence and requests for materials should be addressed to A.Y.

Publisher's note: Springer Nature remains neutral with regard to jurisdictional claims in published maps and institutional affiliations.

© The Author(s), under exclusive licence to Springer Nature Limited 2019